SAND2021-3240J

Modelling Yield Cap Evolution in Sandstone based on Brittle Creep Experiments

Choens, R.C.[a], Bauer, S.J[a]., Shalev, E.[b], and Lyakhovsky, V.[b]

[a] *Sandia National Laboratories, Albuquerque, New Mexico, USA*
[b] *Geological Survey of Israel, Jerusalem, Israel*

Corresponding Author:
R. Charles Choens II
Rcchoen@sandia.gov
Sandia National Laboratories

ABSTRACT: The Zenifim Formation is being considered as a potential disposal formation for a deep borehole nuclear repository concept in Israel. Site selection and repository construction are intended to ensure that waste is separated from circulating groundwater, but long-term deformation of the wellbore could potentially create fluid flow pathways. To understand how time-dependent rock strength could affect wellbore stability, we conducted creep tests under low to moderate confining pressures on retrieved core from the Zenifim formation. During creep, samples strain slowly as gradual damage accumulation progressively weakens the samples. Failure eventually occurred through the near-instantaneous formation of a shear fracture. Experimental results were used to calibrate a continuum damage poro-elastic model for sandstones. The calibrated damage-poro-elastic model successfully simulates different types of loading experiments including quasi-static and creep. The state of strain in experiments is close to yield during loading as the yield cap continuously evolves with damage accumulation. For creep tests, most damage occurs during triaxial loading. Minor damage accumulation occurs under constant load until the final stage of creep, where damage accelerates and promotes unstable fracturing.

1. Introduction

The Israeli Atomic Energy Commission is interested in disposing of nuclear waste in a long-term geologic repository. Due to the nature and quantities of waste, a deep borehole repository concept is being considered as a potential repository candidate. In this repository concept, a large diameter wellbore over 40 cm would be drilled to a depth of a few kilometers to create a storage zone for nuclear waste [1-5]. Waste would be contained by a combination of packaging, wellbore cements, bentonite clays, asphalt, and backfill [1, 4]. Proper site selection and repository construction, with natural and constructed barriers, are crucial to ensure that radiation would not be exposed to the near surface environment.

The Zenifim Formation is being considered as a potential disposal formation and based on the deep borehole concept (e.g. Arnold et al, 2011), the Zenifim is an ideal disposal candidate. The formation is a fine grained, well-cemented, low porosity, low permeability arkosic sandstone that overlies the basement [6]. The depth to the top of the Zenifim formation is within three to five kilometers of the surface in the Negev Desert [7]. The measured thickness of the Zenifim formation is several hundred meters to kilometers, but exact thickness is unknown as the bottom of the Zenifim formation has not been reached from various exploration wells in Israel [6]. The formation is Precambrian in age and is not associated with any regional petroleum systems, minimizing the potential for accidental human intervention [6]. Initial mechanical characterization of cores taken from depth in the Zenifim formation shows in-situ failure strengths of 400-600 MPa with low permeability [8].

Even in the absence of natural fractures, fractures could be potentially induced as borehole breakouts and drilling induced tensile fractures. Borehole breakouts are areas of compressive fracture

that were first observed in deep oil wells due to advances in dipmeter tools [9-11]. These zones of fractures are a common occurrence in stressed boreholes and can be a useful tool to determine the in-situ stress state [12, 13]. Breakouts occur due to elevated stress concentrations at the face of the wellbore resulting from the removal of material (e.g., Zoback, 2010). Depending on the rock type, breakouts manifest through extensile and shear microcracks around the borehole that link together to form either sharp V-shaped breakouts or rounded dog-eared shaped breakouts [14-19]. The stress concentrations around the borehole can also create tensile stresses that result in extension cracks in the vicinity of the borehole that are aligned with in situ stress orientation [20]. Both breakouts and drilling induced tensile fractures occur along the length of the wellbore, covering depths of the wellbore greater than a kilometer with individual breakouts reaching over a hundred meters in length [20, 21]. In a deep borehole repository in a low permeability formation, the development of fractures along the wellbore would create a possible fluid pathway that could extend to shallower depths in the subsurface. Initial installation of waste would be designed to prevent the development of a fracture network along the borehole, including borehole breakouts and drilling induced tensile fractures. Any breakouts that might occur during the creation of the repository would be sealed after emplacement of waste during the installation of the repository seals.

Long-term deformation of the wellbore could potentially create fluid flow pathways after seal emplacement. Repeated observations in uncased wellbores have observed increases in borehole breakouts over time due to a variety of mechanisms [22-24]. In soft clay rich sediments and shales, breakouts growth was due to slow pore pressure migration and equilibration due to low permeabilities [23, 24], and in crystalline rocks in the German Continental Deep Drilling Program, KTB, borehole, breakouts growth was due to changes in mud chemistry, circulation pressure, and pressure equilibration in fractures lining the borehole [22]. Modelling studies have demonstrated that time-dependent creep can be active at the borehole and result in growth of breakouts [25].

Previous experimental studies have shown that the long-term failure of rocks is highly dependent on applied differential stress, confining pressure, temperature, and chemical environment. Time-dependent behavior is typically investigated using creep experiments, where a sample is loaded to a set differential stress and allowed to deform until failure. Increasing the differential stress at a given confining pressure on the sample for the creep phase of the experiment has been shown to increase strain rates and reduce time to failure [26-31]. Practically, applied creep stresses should be a very high percentage of the short-term failure strength, otherwise time to failure would be too long for laboratory investigations [26]. Changing the confining pressure for creep experiments changes the observed relationship for time to failure and stress sensitivity [26, 28, 29, 32]. Increasing confining pressure typically increases short term failure strength, microcracking, and the amount of inelastic strain prior to

failure [33]. In creep experiments increases in time to failure are observed at higher confining pressures even when loaded at creep stresses at similar percentages of short-term failure levels [26, 32]. Stress sensitivity, or changes in time to failure with creep stress levels, also decreases with increasing confining pressure [26, 29]. Experiments have also demonstrated that creep is temperature dependent [26, 34, 35]. Increasing the temperature by 50°C in Etna basalt increases creep strain rates and increasing temperature by 200°C in Barre granite reduces the time to failure by over an order of magnitude [26, 35]. Increasing temperature by 50°C in porous sandstones increases creep strain rates by over two orders of magnitude [34]. Chemical environment can also affect creep behavior, as samples of Westerly granite at 200°C saturated with water failed three orders of magnitude faster than samples at ambient humidity levels [35]. A concern for a deep borehole repository is that the in-situ conditions associated with the deep burial depth of the storage zone, combined with the disturbed stress state around the borehole, could create favorable conditions for brittle creep over the life of the repository.

Matching the long-term behavior of interest to a wellbore application must be able to account for gradual evolution of rock properties due to accumulation of microcracks and porosity change. Experimental results from laboratory compression tests on rocks and geomaterials can be described by a number of failure criteria: Mohr-Coulomb, Hoek-Brown, Lade, Wiebols and Cook, Griffith Mogi, Drucker-Prager, and others [20, 36, 37]. These criteria are able to describe failure strength of the material as well as the orientation of resulting fractures, and in particular, elastoplastic formations based on bifurcation analysis have shown great ability to predict the onset of different modes of failure in porous sandstones [38-49]. These criteria define the behavior of rocks in terms of stresses, but neglect state of strain, loading history, deformation mechanisms, deformation rates, and the initial state of the material. Stress state formulations are typically not able to link failure strength and pre-existing microcracks, voids, or other flaws [50-52]. One approach to incorporate time dependent behavior is to use models based on damage theories first developed by Kachanov (1958) [53]. Modeling creep using damage rheology was successful in predicting primary, secondary, and tertiary creep [54, 55]. Incorporating thermodynamically based formulation for the poro-elastic media [56, 57] with developed damage models leads to a system of coupled kinetic equations for damage and porosity [58, 59]. These models have shown the ability to match the rate dependent deformation of porous sandstones and the development of hydraulic fractures around wellbores at in situ stresses [60, 61].

To understand potential damage induced around a wellbore based repository, this manuscript and a companion manuscript, Shalev et al., 2021, use geomechanics experiments to calibrate damage-poro-elastic models. In Shalev et al., 2021, we focus on the damage induced by geometric effects in a 3D simulation. In this manuscript, we focus on the evolution of damage and time dependent behavior of the Zenifim formation through observed creep tests with associated acoustic emission behavior. At high and

low confining pressures, samples strained slowly upon reaching the creep stress due to gradual damage accumulation that progressively weakened the samples. Failure occurred through the near-instantaneous formation of a shear fracture. The damage-poro-elastic models are calibrated using standard triaxial compression experiments, and when applied to creep experiments, the models can match the observed strain behavior and the damage accumulation inferred from acoustic emission. We quantify the extent of each stage of creep by analyzing the role of the interplay between the evolution of damage, strain, and yield cap.

2. Model Theory

The continuum damage-poro-elastic model considers two thermodynamic state variables, i.e., porosity and damage intensity coupled by kinetic relations [60]. For low porosity crystalline rocks, volumetric deformation expressed by the porosity change is small and might be neglected for practical applications. The damage variable representing subcritical crack growth from the very early stages of loading, material degradation due to increasing crack concentration, macroscopic brittle failure, post failure deformation, and healing. The damage increases toward a critical level, leading to brittle instability and an accompanying macroscopic failure event [61, 62]. The extended poro-elastic model with two damage and porosity variables, addresses three different deformation regimes that are defined by two envelopes (Fig. 1). The heavy line schematically defines the yield cap and the straight-dotted line represents the transition between compaction and dilation (C-D), i.e., the onset of the inelastic porosity increase. These lines define three zones in the differential-volumetric strain diagram: [60]

1. Regime I, beneath the yield cap, represents conditions of quasi-elastic deformation accompanied by material strengthening associated with crack closure and compaction (porosity decrease).

2. Regime II is associated with stress-induced damage (microcracking) and porosity decrease. The damage accumulation starts when the loading crosses the yield cap. Distributed microcracking and grain crushing enable sliding along newly created internal surfaces, collapse of pore space, and change of grain packing. These processes are most prominent under high confining pressures usually treated as cataclastic flow associated with compaction.

3. Regime III is associated with accelerated damage accumulation leading to the macroscopic brittle failure. When the loading is beyond the C-D transition, intensive damage accumulation along with significant differential strains lead to material dilation (porosity increase). Damage increase is bounded by a certain critical value (damage, α equals 1) corresponding to macroscopic brittle failure, dynamic stress drop, and fast conversion of the differential elastic strain into plastic strain components.

While the rock is loaded beyond the yield cap, inelastic compaction acts to reduce elastic volumetric strain and at the same time to expand the yield cap (strengthening). The rates of compaction, damage accumulation, and cataclastic flow depend on the distance between the strain state and the yield cap. On-going load along with the evolving material properties tend to increase the distance between the strain state and the yield cap. On the other hand, this distance is reduced due to expansion of the yield cap. If the yield cap grows fast enough to keep pace with the strain state, their rates equilibrate reaching a steady state in which the yield cap grows at the same rate as the loading rate. Such equilibrium conditions could sustain for a long time being accompanied by slow material degradation and creep. Below we briefly present the main model equations slightly modified after Lyakhovsky et al. (2015).

The stress strain relation for damaged material is given by

$$\sigma_{ij} = \left(\lambda I_1 - \gamma\sqrt{I_2}\right)\delta_{ij} + \left(2\mu - \gamma\frac{I_1}{\sqrt{I_2}}\right)\varepsilon_{ij} \tag{1}$$

where $I_1 = \varepsilon_{kk}$ and $I_2 = \varepsilon_{ij}\varepsilon_{ij}$ are the first and second invariants of the elastic strain tensor, which is the difference between the total, ε_{ij}^t, and irreversible, ε_{ij}^{ir}, strain components $\left(\varepsilon_{ij} = \varepsilon_{ij}^t - \varepsilon_{ij}^{ir}\right)$. The total strain tensor is expressed through the displacements, $\varepsilon_{ij}^t = 1/2\left(\partial u_i/\partial x_j + \partial u_j/\partial x_i\right)$. The deviatoric part of the irreversible strain is accumulated during the viscous, Maxwell-type, relaxation, while change of the volumetric component is equal to the porosity change ($\varepsilon_{kk}^{ir} = d\theta$). λ and μ are the Lamé parameters of linear Hookean elasticity and γ is a third modulus for a damaged solid, which changes from zero for damage-free rock to its maximal value γ_1 at failure. The damage accumulation in regime II, which is relevant for the present study, is given by the kinetic equation:

$$\frac{d\alpha}{dt} = C_d\left[D_1 e^{D_2\alpha}(-I_1)^{n+1}\sqrt{I_2} + I_2(\xi - \xi_0)\right] \tag{2}$$

In the specific model application of this study, the porosity change (irreversible volumetric strain) is small. Nevertheless, for the complete model formulation we present the kinetic equation for the evolving porosity:

$$\frac{d\theta}{dt} = C_d D_1 e^{D_2\alpha}(-I_1)^{n+1}\sqrt{I_2}\frac{\gamma_1}{P_e}I_2(\xi - \xi_0) \tag{3}$$

where C_d is the kinetic coefficient, the strain invariant ratio, $\xi = I_1/\sqrt{I_2}$, the critical strain invariant ratio, ξ_0. The competition between first positive term in square brackets of the damage kinetic equation (2) ($D_1 e^{D_2\alpha}(-I_1)^{n+1}\sqrt{I_2}$) and the second negative ($\xi < \xi_0$) term ($I_2(\xi - \xi_0)$) controls the onset of the damage accumulation and defines the shape of the yield cap. The kinetic equation (3) share the similar terms, but instead of their sum, they are multiplied. Below the compaction-dilation transition ($\xi = \xi_0$), this equation always predicts small porosity reduction, or compaction. It was shown in [60] that the power index n>1 (n=2 for all model runs), define the shape of the yield cap, which changes size in almost self-

similar manner with the value of the damage-dependent function $D_1 e^{D_2 \alpha}$ adopted in the present formulation. For negative D_2 value, the first term in (2) decreases with damage increase, leading to the increase in the yield cap toward the straight line of the compaction-dilation transition (Fig. 1). This is the major modification of the kinetic equations of [60], which incorporate the damage-controlled material memory in the original formulation. Analytical solutions of the reduced 1-D formulation discussed in [72] show that the model with the damage-controlled material memory enable reproducing the Kaiser effect.

Substituting $d\alpha/dt = 0$ into (2) leads to the equation which defines the onset of damage accumulation or the shape of the yield cap. This equation connects the volumetric strain with the strain invariant ratio and its solution may be written in two ways:

$$\xi = \frac{\xi_0}{1 - D_1 e^{D_2 \alpha} (-I_1)^n} \tag{4a}$$

or

$$I_1 = -\left(\frac{\xi_0 - \xi}{\xi \cdot D_1 e^{D_2 \alpha}}\right)^{1/n} \tag{4b}$$

This solution shows that for zero D_2 value the yield cap does not depend on the damage level, while increased negative values correspond to its expansion with the damage growth.

Following the onset of positive damage evolution, the creep is modeled as gradual accumulation of irreversible strain components, ε_{ij}^{ir}. Damage increase means nucleation and growth of micro-cracks. A fracture recovers all the elastic component of deformation leaving irreversible strain upon unloading. Comparisons between theoretical predictions, observed deformation and acoustic emission from laboratory experiments in granites and sandstones, led Hamiel et al. to suggest that the accumulation rate of the damage-related irreversible deformation is proportional to the rate of damage increase:

$$\frac{d\varepsilon_{ij}^{ir}}{dt} = C_v \frac{d\alpha}{dt} \tau_{ij} \tag{5}$$

where C_v is a material constant and $\tau_{ij} = \sigma_{ij} - \sigma_{kk}\delta_{ij}/3$ is the deviatoric stress tensor [58]. The compliance or inverse of viscosity ($C_V \, d\alpha/dt$) relates the deviatoric stress to the rate of the irreversible strain accumulation. The positive material parameter C_V with inverse of stress units is assumed to be constant and is constrained using laboratory data. There is no new timescale associated with the rate of irreversible strain accumulation, since it is controlled by the rate of the damage growth.

3. Methods

3.1. Material – Zenifim SS

Experiments were conducted on samples from the Zenifim formation obtained by downhole coring. The Zenifim is Precambrian age arkosic facies that consists of well-cemented sandstones with thin layers of siltstones and mudstones with basal conglomerates [6]. The sandstones can be massive, horizontally bedded, or cross-stratified. Compositionally, these arkosic sandstones are 50% feldspar, 40% quartz, and 10% lithics, biotite, chlorite, hornblende [6]. The formation was deposited in onshore to near-shore environments where the depositional sequence transitioned from alluvial fan deposits to braided alluvial plain to tidal flat environments due to marine transgressions and tectonically related basin subsidence [6]. The samples tested in this study show a change in material at the bottom of the core to a lighter colored lens from reddish cross-stratifications (Fig. 2). Fine, weakly cemented sub horizontal bedding planes are present in the top portion of the sample. Also present in the samples are fine scale fractures that have been recemented. Thin section observations of samples show additional anisotropy on the grain scale (Fig. 3). Micrographs shows elongate quartz and feldspar grains preferentially aligned with mica flakes (Fig. 3a). Observations also show different types of cementing phases in the samples. The primary cement phase is a fine-grained matrix of hematite, chlorite, and clays (Fig. 3b). Also present in the sample to a lesser extent is an authigenic calcite cement (Fig. 3c). Thin hematite grain coatings are present on almost all grains, suggesting that these cementation phases formed later.

3.2. Experimental Method

Zenifim core samples were prepared as 24.4±0.4 mm diameter cylindrical cores, 56.2±0.7 mm in length, cored perpendicular to the bedding orientation. Samples were end ground for parallelism using a precision surface grinder. A series of preliminary experiments were performed on parallel and perpendicular cores of Zenifim sandstone to define the failure envelope. These experiments were intended to determine axial stress levels for consistent creep behavior in later tests, but heterogeneities in strength prevented accurate picks of creep stress. Samples were instrumented with 2 strain gage rosettes, 2 axial LVDTs, and 4 AE pins. Strain gages were mounted directly onto to the samples. AE pins were affixed into brass guides and epoxied to the surface of the sample. These experiments were performed using an older, less sensitive AE system than the later creep tests, and combined with the deficiencies in the mounting method, the AE data from these preliminary experiments are not included here as they are an order of magnitude less in number than the creep results. Samples were jacketed with UV cure urethane. Samples were deformed at confining pressures of 7, 50, 100, and 200 MPa. Six experiments were performed in total, with repeats at 7 and 100 MPa confining pressure. Small loading cycles were performed during these conventional triaxial experiments to assist with model validation.

Creep samples utilized a different jacketing procedure to increase coupling between AE pins and the sample due to poor results in preliminary tests. Samples were jacketed using 0.13 mm thick annealed

copper foil. A rectangular piece of copper foil was wrapped around the sample, the seam was covered with a small strip of copper and soldered with Wood's metal. Copper foil caps with pre-rolled edges were soldered onto the ends of the sample. The jacket was set using 500 PSI nitrogen to compress the jacket and check for leaks. To monitor the evolution of damage during experiments, samples were instrumented with 8 Dynasen© piezoelectric transducers to monitor acoustic emissions (AEs). The pins were mounted onto the samples using Wood's metal. These pins have a linear output up to 2 kbar with a 0.1 microsecond response time and a natural frequency of 2.5 MHz [63]. Three equally spaced pins were mounted on the top and bottom of the sample, and two additional pins were mounted in the center of the sample. Samples were instrumented with two strain gage rosettes (SG1 and SG2), each with an axial and radial strain component. Samples were coated with a layer of UV cure urethane. Linear variable displacement transducers (LVDT) were used to measure axial deformation by using screw mounted rings affixed to the sample endcaps (LVDT1 and LVDT2). Issues with electrical connections prevented all the instrumentation from preforming properly during testing, although each sample had at least one functional LVDT and strain gage rosette. For sample SC-4, LVDT 2 and SG2 did not perform properly. During creep however, SG2 did start to function properly. For sample SC-7, the lateral component of SG1 did not function properly.

Creep samples were deformed at 6.9 and 200 MPa confining pressure, P_C. Samples were loaded hydrostatically to the desired confining pressure and deformed at an axial compression rate of 5.7×10^{-4} mm/sec (strain rate $=2.3 \times 10^{-5}$ sec^{-1}) until the target differential stress was achieved. Creep tests are typically loaded rapidly to a predefined creep load, but the highly heterogeneous nature of the samples precluded using a predefined creep load. Samples were loaded at a typical compression rate and the creep load was set based on apparent yielding observed in sample strain and AE response. Sample SC-4 was loaded to 245.7 MPa differential stress ($\Delta\sigma$), sample SC-7 was loaded to 717.2 MPa $\Delta\sigma$, and these axial stresses were maintained within 0.2 MPa throughout the experiment (Table 1). Samples SC-4 and SC-7 exceeded the failure strength of previous test before yielding.

During creep testing, AE was monitored using a Mistras© Micro-II Express system with an Express-8 eight channel AE board. Signals were preamplified with a 60 dB gain, and bandpass filtered for a range of 100 kHz to 1000 kHz. An AE hit is defined and was recorded when the signal on one channel crossed a predetermined threshold. The test at 6.9 MPa P_C had a 30 dB threshold, and the test at 200 MPa P_C had a 24 dB threshold. In postprocessing, the threshold was lowered by 5 dB for each waveform after filtering out background noise to increase accuracy when selecting first arrival. Displacement of the hydraulic actuator, axial load, confining pressure, LVDT displacements, and strain gage deformation were recorded by the frame controlling software at 1 second intervals, although the timing interval was increased to 5 minutes for the majority of the creep phase of SC-4. Strain gage deformation was also

recorded as parametric inputs on the AE system, where these values were recorded with each AE hit. This created a record that was very sporadic at the beginning of triaxial loading (i.e. minimal AE hits) but exhibited extremely high resolution at failure.

3.3. Modelling Methods

Modelling the laboratory experiments was performed by explicit-in-time solution of the kinetic equations (2, 3) and (5) for a given set of the material parameters. The model input is the loading or stress components, and those values combined with the elastic moduli values from the previous step are used to predict the elastic strain components for the current time step using equation (1). If the obtained state of strain falls below the yield cap (4), the elastic properties and irreversible strain components remain unchanged. When the strain state is above the yield cap, new damage and porosity values were explicitly calculated using equations (2, 3), and then the obtained rate of damage accumulation is used to calculate the new irreversible strain (5). The total strain at every time step was calculated taking the sum of the elastic and irreversible strain components as well as the porosity change for the volumetric components. The obtained stress-strain relationships are compared with the experimental observations. We did not apply any automatic optimization procedure to define the best fit by changing the model parameters. We ran many direct simulations with the goal to obtain a reasonable fit to the stress-strain relationships within relatively small variations of the model parameters for different experiments.

4. Results

4.1. Experimental Results

Conventional triaxial experiments failed by the development of through going shear bands. Differential stress at failure increased with increasing confining pressure, but failure strength is similar for experiments performed at 100 MPa and 200 MPa P_C (Fig. 4). With the exception of the experiment at 100 MPa P_C, the samples showed very little inelastic strain prior to failure. The samples did not show any significant strain softening post yielding. The 100 MPa P_C sample showed clear softening and appreciable roll over in the stress strain curve prior to failure (Fig 4a). Failure strength does not form a linear relationship with mean stress (Fig. 4b).

Samples SC-4 and SC-7 were allowed to creep until failure by the development of a through-going shear fracture (Fig. 5). For the experiment conducted at 6.9 MPa P_C, the sample crept for 2129659 seconds (591.57 hours) until failure, and for the experiment conducted at 200 MPa P_C, the sample crept for 40539 seconds (11.26 hours) until failure (Table 1). SC-4 deformed slightly during the creep phase, and SC-7 noticeably strained during the creep phase. Fractures for the two samples were qualitatively similar in terms of orientation and apparent thickness despite large differences in confining pressure,

strain, creep time, and AE activity (Fig. 5-8; Table 1). In SC-4, the fracture formed at the top of the sample, and in SC-7, the fracture formed at the bottom of the sample.

Samples SC-4 and SC-7 were loaded until the sample yielded as indicated by changes in strain behavior and AE response. In SC-4, volume strain shows the sample had stopped compacting but had not yet started to dilate at onset of creep (Fig. 6a). At this low confining pressure, the response of the sample is very brittle and fails without accumulating significant inelastic strain. In SC-7, volume strain shows the sample had started to dilate at the onset of creep (Fig. 6b). For both samples, strain measurements based on LVDTs and strain gages are similar, but strain gages show slightly more strain (Fig. 6).

Despite large differences in creep times, both experiments were able to capture the three stages of creep: primary, secondary, and tertiary creep (Fig. 7). Creep strain rates decreased over time, until an increase in strain rate from the last stage of creep through failure (Fig. 7). Primary and secondary creep are observed in the lateral strain response for SC-4 before fracture occurs, and failure occurs suddenly without increased yielding (Fig. 7a). Three stages of creep are observed in the lateral strain response of SC-7 (Fig. 7b). Different behavior can be observed in the lateral and volume strain behavior of the samples. Both samples had yielded prior to the onset of creep, and both samples continue to dilate during the hold period (Fig. 7). Sample SC-7 continues to dilate at failure, but SC-4 starts to compact at failure. This is likely due of observable tertiary creep on the lateral component of the strain gage.

Strain gage data recorded by the AE system presents a high-resolution record of deformation leading up to failure. In the 3 seconds before and after failure, the frame controlling software set to a 1 Hz sampling rate recorded 6 data points; the AE system recorded over 16000 and 120000 data points for SC-4 and SC-7 (Fig. 8). The frame software operates at a set recording frequency to produce a consistent data record. The AE system recorded strain gage values with every hit, which lead to a sporadic data record during creep but a very dense record during periods of high damage accumulation. The high-resolution data shows that strain accelerates within 1 second of fracture. For sample SC-4, axial strain increases and lateral strain decreases (Fig. 8a). At failure, the sample begins to dilate despite the compaction seen in tertiary creep (Fig. 7a, 8a). Strain on SG1 rapidly maxes out, indicating it has been sheared by the fracture formation. Strain on SG2 temporarily decreases after failure, but strain is quickly recovered and final magnitude is similar to axial LVDT values (Fig. 6a, 8a). The temporary decrease on SG2 was not captured by the 1 Hz sampling rate of the frame software. Smaller axial responses are seen in sample SC-7 (Fig. 8b). Axial strain increases on SG1 and decreases on SG2. Lateral and volume strain significantly decreases at failure of the sample. This data (Fig. 8) highlights the rapid changes that can occur immediately preceding the development of a through-going shear fracture.

4.2 Acoustic Emission Activity

Acoustic emission activity began during hydrostatic loading for both samples. Some AEs were observed in SC-4, but significant AEs were observed in SC-7 due to the high applied confining pressure (Fig. 6c, d). AE accumulation was slower during the initial triaxial loading phase for both samples but increased with increasing differential stress. When AE rates started to noticeably increase during loading, this increase was used an indicator to start the creep portion of the test. In SC-4, AE hits accumulated steadily during creep and AE rates remained at a constant low level over the prolonged creep period (Fig. 6c, 7a). AE hits and AE rates surged at failure after briefly slowing down (Fig. 6c, 7a). In SC-7, AE hits accumulated at a constant level during the first two stages of creep. AE hits began to increase during tertiary creep, and a large surge in hits and orders of magnitude increase in AE rate occurred at failure (Fig. 6, 7). SC-7 had substantially more AE hits than SC-4 (Table 1).

4.3 Model Results and Model Experiment Comparisons

Figure 9 presents stress strain curves for the different modeling results, which are in good agreement with the experiments (Fig. 4, 9). Calibrated modeling parameters (Table 2) include the elastic moduli, λ and μ, controlling the slope of the stress-strain curve at early stages of the loading, below the yield cap. During loading, the yield cap evolves with accumulated damage (Fig. 1). The absence of the acoustic emissions during small unloading and re-loading cycles shown in the stress-strain curves (Fig. 9 a, b) suggests that in these experiments the strain state is always very close to the yield cap. Plotting the loading path (Fig. 10a, b) and using the onset of the unloading cycles as a proxy for the location of the yield cap provides the constraint for the parameters ξ_0, D_1, D_2, controlling the shape of the yield cap. The kinetics of damage accumulation (controlled by C_d value) and the resulting evolution of the yield cap are keeping pace with the strain accumulation. During the long creep period (Fig. 9c, d), the stresses are held constant and the strains and the yield cap keep slowly evolving together (Fig. 10c, d). The calibrated parameters were constrained by a series of direct stress-strain calculations (red lines in Fig. 9) with pre-defined parameters. The record of the time dependent stress values applied during the laboratory experiment was used as the modelling input. For every consecutive time step we calculate the elastic strain by inverting stress-strain relation (1) using elastic moduli from the previous step. The calculated elastic strains were used for direct calculation of the new values of the damage (2) and the irreversible strain components (5). The later together with the elastic strain components give the total strain compared with the measured strain on the stress-strain plot (Fig. 9). For every test, calculations were repeated until the calculated stress-strains fitted the experimental results.

These experiments involve three stages: accelerated acoustic emission during active loading that declines to steady state (primary creep), minor acoustic emission during creep (secondary creep), and sharply accelerated acoustic emission during unstable fracturing (tertiary creep) (black line in Fig. 11a).

Measured and simulated axial strain show these three stages. Lateral strain shows the same pattern. From the simulation results it is possible to calculate the proximity of the yield cap to strain conditions (black line in Fig. 11b). During active loading, the yield cap cannot keep up with the increasing damage. Most of the damage is accumulated during this stage (red line in Fig. 11b) and this is similar to the acoustic emission activity (black line in Fig. 11a). During creep, the sample is always slightly above yield, and damage accumulation is minor: damage changes from 0.26 to 0.29. At the last stage, the yield cannot keep up with the evolving strain and the difference between the strain and the yield cap increases promoting unstable fracturing. The proximity of the yield cap to the strain state ($\Delta\varepsilon$) dictates the rate of the deformation. High deformation rates are expected when the strain state is far above the yield cap (large $\Delta\varepsilon$), as in the active loading stage. Due to the exponential relation between damage and the yield cap, deformation rates are also dependent on the damage of the rock. High deformation rates are expected at high damage states (unstable fracturing). The presented model is one element with no spatial dimensions and cannot simulate the stage of damage localization and therefore the model is not fitted for the unstable fracturing phase. At this phase, three-dimensional modeling is required.

5. Discussion

The creep stresses for SC-4 and SC-7 were originally intended to be 95% of the failure stresses observed in the conventional triaxial experiments. However, the samples did not show appreciable yielding at these levels, and loading continued until the samples had noticeable inelastic strain and elevated AE activity. The creep level for both experiments was higher than conventional failure stresses (Fig. 4b, 12). SC-7 creep stress was significantly higher, and the long creep time of SC-4 suggests the creep stress could have been higher without premature fracturing of the sample. The creep experiments were also slightly stiffer than the conventional experiments (Fig. 12). It is not clear why creep samples were stronger than conventional triaxial experiments. It is possible that cyclic loading may have prematurely weakened samples, but observed difference between creep and conventional tests are far greater. The differences in strength are likely due to inherent heterogeneities in strength, despite samples coming from the same section of core. Accumulated axial and lateral strain at fracture for experiments conducted at 6.9 MPa P_C is similar for all three experiments. SC-4 is the only experiment at 6.9 MPa P_C that shows dilation, which occurred in the creep phase (Fig. 12a). The results suggest that dilatant behavior associated with shear fracturing are not observed in the conventional experiments likely due to sudden onset of failure and brittle behavior, and dilation occurs in the SC-4 due to the low creep levels that allow for gradual damage accumulation. SC-7 showed significantly more strain than the previous experiment at 200 MPa P_C. Axial and lateral strain at the onset of creep was equal to the total strain in the previous experiment, and SC-7 continued to deform during creep. The previous sample compacted

throughout the experiment; SC-7 began to dilate prior to the onset of creep and continued to dilate during creep (Fig. 12b).

The observed trends of AE activity are consistent between the two experiments, with higher AE activity in SC-7. In both tests, low levels of AE activity are observed during hydrostatic and triaxial loading, and the majority of AE hits are observed during the creep phase. The timing of increased AE activity during creep coincides with increase in strain and strain rates. Axial, lateral, and volume strain all increase near failure, and because strain data is recorded for each AE hit on the AE system, strain gage data recorded on the AE system show a significant peak in the seconds leading to failure. Similar AE activity has been observed in creep experiments on sandstones and crystalline rocks [26, 28, 29, 34, 64].

The creep experiments on Zenifim sandstone presented here show similar behavior to other creep experiments on porous and crystalline rocks conducted at similar conditions [26]. Both Zenifim creep tests displayed three distinct stages of strain rate: a primary stage of creep where strain rates decelerate, a secondary stage where strain accumulates at a steady value, and a tertiary creep phase where strain rates accelerate preceding sample failure (Fig. 7). Due to the differences in strength from the creep and quasi-static experiments, it was difficult to start the creep portion of the experiment at a consistent percentage of failure (Fig. 12). Consequently, the time to failure varied greatly between SC-4 and SC-7. SC-4 crept for 24 days, and SC-7 crept for just over 11 hours. Experiments on Barre granite have demonstrated that changes for time to failure for different effective pressures can be explained by changes in failure strength associated with different effective pressures as well as increasing inelastic strain accumulation prior to failure [26, 32]. This would suggest that SC-7 should have had a slightly longer time to failure if the creep stresses were equal percentages of failure. Due to the highly variable nature of Zenifim sandstone, it was not possible to accurately pick a consistent creep stress as a percentage of failure stress between the two samples. The increased ductility at 200 MPa P_C allowed us to pick a creep stress closer to failure than 6.9 MPa P_C experiment.

Laboratory experiments in porous rocks show evidence of strain hardening and yield cap growth attributed to plasticity and porosity loss (e.g., Baud *et al.* 2006; Bedford *et al.*, 2018; Tembe *et al.* 2007; Wong and Baud, 2012 [38, 48, 65, 66]). Grueschow and Rudnicki (2005) discussed different models of the evolving yield cap [67-69] and suggested a constitutive model connecting between the growth direction of the yield cap and tendency towards different failure modes. This is also reflected in the results of models that attribute different deformation patterns to the change in the elastic properties and yield cap evolution due to porosity change [60, 70, 71]. The modified Lyakhovsky et al [60] model suggests the damage-dependent growth of the yield cap as it is schematically shown in Figure 1. The modified formulation incorporates damage-controlled rock memory which allows for reproducing the Kaiser effect [72]. Results of this study show that for the Zenifim arkosic sandstone under slow loading rates, the yield cap closely

follows the ongoing axial load (Fig. 10). Therefore, during most of unloading and reloading cycles (Fig. 9a, b) the samples are below yield and the model predicts no damage growth, which is compatible with no AE in the experiments. These cycles are completely reversible which also indicates that it is performed in the elastic regime below the yield cap. While strain approaches unstable fracturing (Regime I in Fig. 1), strain hardening is less efficient which causes a deceleration of the yield cap growth. In the model, this feature is described by exponential dependence of the yield cap on damage with negative D_2 value in (2). Therefore, the strain state of the last cycles in both Figure 10a and 10b start above the yield cap and damage accumulates even during the unloading causing non-reversibility of the strain.

The model predicts primary, secondary, and tertiary creep and highlights the mechanics of each stage. Prior to the creep stage, the sample is beyond the yield cap defined by the onset of AE. At the onset of creep, the stress is held constant, but the strain continues to evolve. The model shows that during primary creep, the yield cap evolves towards the strain state of the sample (Fig. 11b). $\Delta\varepsilon$ is a measure of the distance in strain space between the strain of the sample and the location of the yield cap. The evolution of the yield cap towards the strain of the sample decreases during primary creep. Once the yield cap gets close to the strain ($\Delta\varepsilon$~0), creep strain rate slows. At this stage, the sample is only slightly above yield. The yield cap moves slowly towards the strain state of the sample, but the strain is reacting to the continuous change of damage and mechanical moduli. The rate of deformation depends on the distance between the strain state and the yield cap as well as the value of damage. High damage causes high deformation rates. Once damage increases to a high value, deformation accelerates and creep enters the tertiary creep stage (Fig. 11a,b). The interplay between the evolution of damage, strain, and yield cap controls the extent of the primary, secondary, and tertiary creep.

During the creep stage of the experiments with constant stress conditions, small amount of AE is a manifestation of ongoing fracturing of the samples. In the model it is expressed by slow damage accumulation, changing the elastic properties of the sample and thereby causing changes in elastic strains and accumulation of the irreversible strain. To illustrate the role of damage accumulation during the creep stage, we simplify the stress-strain relation (1) to:

$$\sigma = 2\mu\,(1-\alpha)\varepsilon = Constant \tag{6}$$

Taking the time derivative leads to expression for the change in the elastic strain:

$$\dot{\varepsilon} = \frac{\dot{\alpha}}{(1-\alpha)}\frac{\sigma}{\mu} \tag{7}$$

which means that the elastic strain changes proportionally to the rate of damage accumulation. This is the reason for the small changes in the total strain during creep. In the case of small C_v values in (5), this mechanism becomes dominant. This is clearly shown by the red line in Figure 10d for the 200 MPa test.

The change in the elastic strains under 6.9 MPa (Fig. 10c) is very small and could be only recognized in the insert.

Viscous flow, which describes the relaxation of shear stress, is traditionally addressed as a temperature activated mechanism. We suggest that during creep stage, the accumulation of irreversible strain decreases shear stress similar to viscous flow. The creep mechanism is associated with ongoing fracturing, nucleation and growth of micro-cracks (damage increase) that react to the imposed shear strain and cause micro stress drops (AE events) that reduce shear stress.

6. Conclusions

This study investigated the damage evolution and time dependent behavior in a low porosity sandstone through creep experiments, conventional triaxial experiments, and numerical analyses. Experiments were conducted on samples from the Zenifim formation obtained by downhole coring. We tested fine grained, well cemented, horizontally bedded arkosic sandstones at two different confining pressures, 6.9 MPa and 200 MPa, for creep tests. Samples were hydrostatically loaded to the confining pressure, axially loaded at a strain rate of $1x10^{-5}$ sec^{-1} to the creep stress and allowed to deform until failure. For the experiment conducted at 6.9 MPa P_C, the sample crept for 2129659 seconds before failure. For the experiment conducted at 200 MPa P_C, the sample crept for 40539 seconds before failure. Despite the large difference in confining pressure and creep time, the samples deformed and failed in similar ways. Both samples showed primary, secondary, and tertiary creep. High resolution strain gage data recorded by the AE system shows both samples had an increase in strain rate immediately preceding failure. Both samples failed by the formation of a through going shear fracture with a similar appearance for both samples.

The calibrated damage-poro-elastic model modified after Lyakhovsky et al., (2015), successfully simulates different types of loading experiments including quasi-static and creep. As damage accumulates in the samples, the yield cap evolves to keep pace with strain accumulation. In the quasi-static experiments, the state of strain is above yield during the active loading stage and is below the yield during the unloading-reloading cycles (no AE and damage accumulation). During the secondary creep stage, the state of strain is always slightly above the yield cap causing minor AE and damage accumulation. This secondary creep stage lasts as long as the distance between the state of strain and yield cap remains small. Since the relation between the growth of the yield cap and the damage is exponential, the growth of the yield cap slows down at elevated damage values and cannot keep up with evolving strain leading to tertiary creep stage.

Sandia National Laboratories is a multimission laboratory managed and operated by National Technology & Engineering Solutions of Sandia, LLC, a wholly owned subsidiary of Honeywell International Inc., for the U.S. Department of Energy's National Nuclear Security Administration under contract DE-NA0003525.

SAND2021-

References

1. Arnold B. W., Brady P. V., Bauer S. J., Herrick C., Pye S., Finger J. Reference design and operations for deep borehole disposal of high-level radioactive waste. *SAND2011-6749, Sandia National Laboratories,* 2011.
2. Arnold B. W., Vaughn P., MacKinnon R., Tillman J., Nielson D., Brady P., Halsey W., Altman S. Research, Development, and Demonstration Roadmap for Deep Borehole Disposal. *SAND2012− 8527P. Sandia National Laboratories*, 2012.
3. Brady P. V., Arnold B. W., Freeze G. A., Swift P. N., Bauer S. J., Kanney J. L., Rechard R.P., Stein J.S. Deep borehole disposal of high-level radioactive waste. *Sandia Report SAND2009-4401, Sandia National Laboratories*. 2009.
4. Brady P. V., Freeze G. A., Kuhlman K. L., Hardin E. L., Sassani D. C., MacKinnon R. J. Deep borehole disposal of nuclear waste: US perspective. In *Geological Repository Systems for Safe Disposal of Spent Nuclear Fuels and Radioactive Waste*. Woodhead Publishing. 2017. pp. 89-112
5. Woodward-Clyde Consultants. *Very deep hole systems engineering studies.* ONWI. 1983.
6. Weissbrod T., Sneh A. *Sedimentary and paleogeography of the late Precambrian – Early Cambrian arkosic and conglomeratic facies in the northern margins of the Arabo-Nubian Shield.* Bulletin 87. Jerusalem: Geological Survey of Israel. 2002.
7. Calvo R., Gvirtzman Z.. Assessment of CO2 storage capacity in southern Israel. *Int J Greenh Gas Control*. 2013;14:25-38.
8. Shalev E., Bauer S., Homel M. A., Antoun T. H., Herbold E. B., Vorobiev O. Y., Levin H., Oren G., Lyakhovsky V. Breakout modeling in arkose and granite rocks. *Geomech and Geophs for Geo-Energy and Geo-Resour*. 2021;7:1-23.
9. Bell J., Gough D. Northeast-southwest compressive stress in Alberta evidence from oil wells. *Earth and Planet Sci Letters*. 1979;45:475-482.
10. Gough D., Bell J. Stress orientations from oil-well fractures in Alberta and Texas. *Canadian J Earth Sci.* 1981;18:638-645.
11. Gough D., Bell J. Stress orientations from borehole wall fractures with examples from Colorado, east Texas, and northern Canada. *Canadian J of Earth Sci.* 1982;19:1358-1370.
12. Vernik L., Zoback M.D. Estimation of maximum horizontal principal stress magnitude from stress- induced well bore breakouts in the Cajon Pass scientific research borehole. *J Geophys Res: Solid Earth*, 1992;97:5109-5119.
13. Zoback M. D., Moos D., Mastin L., Anderson R. N. Well bore breakouts and in situ stress. *J Geophys Res.* 1985;90:5523-5530.
14. Choens R. C., Lee M. Y., Ingraham M. D., Dewers T. A., Herrick C. G. Experimental Studies of Anisotropy on Borehole Breakouts in Mancos Shale. *J Geophys Res: Solid Earth.* 2019;124:4119-4141.
15. Ewy R., Cook N. Deformation and fracture around cylindrical openings in rock—II. Initiation, growth and interaction of fractures. in *Int J Rock Mech Min Sci Geomech Abstracts*. 1990. Elsevier.

16. Haimson, B.C., Micromechanisms of borehole instability leading to breakouts in rocks. *Int J Rock Mech Min Sci.* 2007;44:157-173.
17. Haimson B.C., Herrick C. *Borehole breakouts-a new tool for estimating in situ stress?* in *ISRM International Symposium*. 1986. International Society for Rock Mechanics and Rock Engineering.
18. Lee M., Haimson B.C. Laboratory study of borehole breakouts in Lac du Bonnet granite: a case of extensile failure mechanism. in *Int J Rock Mech Min Sci Geomech Abstracts*. 1993. Elsevier.
19. Song I., Haimson B.C. Polyaxial strength criteria and their use in estimating in situ stress magnitudes from borehole breakout dimensions. *Int J Rock Mech Min Sci.* 1997;34:1-16.
20. Zoback, M.D., *Reservoir geomechanics*. 2010: Cambridge University Press.
21. Fordjor C., Bell J., Gough D, Breakouts in Alberta and stress in the North American plate. *Canadian J Earth Sci.* 1983;20:1445-1455.
22. Kessels, W. *Obervation and interpretation of time-dependent behaviour of boreholes stability in the continental deep drilling pilot borehole*. in *ISRM International Symposium*. 1989. International Society for Rock Mechanics and Rock Engineering.
23. Kupferschmied N., Wild K. M., Amann F., Nussbaum C., Jaeggi D., Badertscher N. Time-dependent fracture formation around a borehole in a clay shale. *Int J Rock Mech Min Sci.* 2015;77:105-114.
24. Moore J.C., Chang C., McNeill L., Thu M. K., Yamada Y., Huftile G. Growth of borehole breakouts with time after drilling: Implications for state of stress, NanTroSEIZE transect, SW Japan. *Geochem, Geophys, Geosyst*. 2011;12.
25. Schoenball M., Sahara D.P., Kohl T. Time-dependent brittle creep as a mechanism for time-delayed wellbore failure. *Int J Rock Mech Min Sci*. 2014;70:400-406.
26. Brantut, N., Heap M.J., Meredith P.G., Baud P. Time-dependent cracking and brittle creep in crustal rocks: A review. *J Structural Geol*. 2013;52:17-43.
27. Fujii Y., Kiyama T., Ishijima Y., Kodama J. Circumferential strain behavior during creep tests of brittle rocks. *Int J Rock Mech Min Sci.* 1999;36:323-337.
28. Heap M., Baud P., Meredith P.G., Bell A.F., Main I.G. Time- dependent brittle creep in Darley Dale sandstone. *J Geophys Res: Solid Earth*, 2009;114.
29. Heap M., Baud P., Meredith P.G., Vinciguerra S., Bell A.F., Main I.G. Brittle creep in basalt and its application to time-dependent volcano deformation. *Earth Planet Sci Letters*. 2011;307:71-82.
30. Kurita K., Swanson P.L., Getting I.C., Spetzler H. Surface deformation of Westerly granite during creep. *Geophys Res Letters*, 1983;10:75-78.
31. Sone H., Zoback M.D. Time-dependent deformation of shale gas reservoir rocks and its long-term effect on the in situ state of stress. *Int J Rock Mech Min Sci.* 2014;69:120-132.
32. Kranz R.L., The effects of confining pressure and stress difference on static fatigue of granite. *J Geophys Res: Solid Earth*. 1980;85:1854-1866.
33. Paterson M.S. Wong T.-F. *Experimental rock deformation-the brittle field*. 2005: Springer Science & Business Media.
34. Heap M., Baud P., Meredith P. Influence of temperature on brittle creep in sandstones. *Geophys Res Letters*, 2009;36.
35. Kranz R.L., Harris W.J., Carter N.L. Static fatigue of granite at 200 C. *Geophys Res Letters*. 1982;9:1-4.
36. Colmenares L., Zoback M. A statistical evaluation of intact rock failure criteria constrained by polyaxial test data for five different rocks. *Int J Rock Mech Min Sci*. 2002;39:695-729.
37. Jaeger J.C., Cook N.G., Zimmerman R. *Fundamentals of rock mechanics*. 2009: John Wiley & Sons.
38. Baud P., Vajdova V., Wong T-F. Shear- enhanced compaction and strain localization: Inelastic deformation and constitutive modeling of four porous sandstone*s. J Geophys Res: Solid Earth,* 2006;111.
39. Bésuelle P. Compacting and dilating shear bands in porous rock: Theoretical and experimental conditions. *J Geophys Res: Solid Earth.* 2001;106:13435-13442.

40. Chemenda A.I. Origin of compaction bands: Anti-cracking or constitutive instability? *Tectonophysics*. 2011;499:156-164.
41. Chemenda A.I., Wibberley C., Saillet E. Evolution of compactive shear deformation bands: Numerical models and geological data. *Tectonophysics*. 2012;526:56-66.
42. Issen K.A., Challa V. Influence of the intermediate principal stress on the strain localization mode in porous sandstone. *J Geophys Res: Solid Earth*. 2008;113.
43. Issen K.A., Rudnicki J.W. Conditions for compaction bands in porous rock. *J Geophys Res: Solid Earth.* 2000;105:21529-21536.
44. Olsson W.A. Theoretical and experimental investigation of compaction bands in porous rock. *J Geophys Res: Solid Earth.* 1999;104:7219-7228.
45. Rudnicki J.W. Shear and compaction band formation on an elliptic yield cap. *J Geophy Res: Solid Earth.* 2004;109.
46. Rudnicki J.W. Models for compaction band propagation. *Geol Soc London, Special Pub*. 2007;284:107-125.
47. Rudnicki J.W., Rice J. Conditions for the localization of deformation in pressure-sensitive dilatant materials. *J Mech Phys Sol*. 1975;23:371-394.
48. Tembe S., Vajdova V., Baud P., Zhu W., Wong T-F. A new methodology to delineate the compactive yield cap of two porous sandstones under undrained condition. *Mech Mater*,.2007;39:513-523.
49. Wong T-F., Baud P., Klein E. Localized failure modes in a compactant porous rock. *Geophys Res Letters*. 2001;28:2521-2524.
50. Chen W.-F., Han D.-J. *Plasticity for Structural Engineers*. 2007: J. Ross Publishing.
51. Einav I. Thermomechanical relations between stress-space and strain-space models. *Geotechnique*. 2004;54:315-318.
52. Puzrin A., Houlsby G. Fundamentals of kinematic hardening hyperplasticity. *Int J Sol Struct.* 2001;38:3771-3794.
53. Kachanov L. On the time to rupture under creep conditions. *Izv Akad Nauk SSSR OTN. i8,* 1958;26-31.
54. Amitrano D., Helmstetter A. Brittle creep, damage, and time to failure in rocks. *J Geophys Res: Solid Earth*. 2006;111.
55. Xu T., Tang C. A., Zhao J., Li L., Heap M. J. Modelling the time-dependent rheological behaviour of heterogeneous brittle rocks. *Geophys J Int*. 2012;189:1781-1796.
56. Biot, M.A., Nonlinear and semilinear rheology of porous solids. *J Geophys Res*. 1973;78:4924-4937.
57. Coussy, O., *Mechanics of Porous Continua*. 1995: Wiley.
58. Hamiel Y., Liu Y., Lyakhovsky V., Ben-Zion Y., Lockner D. A viscoelastic damage model with applications to stable and unstable fracturing. *Geophys J Int.* 2004;159:1155-1165.
59. Hamiel Y., Lyakhovsky V., Agnon A. Coupled evolution of damage and porosity in poroelastic media: theory and applications to deformation of porous rocks. *Geophys J Int*, 2004;156:701-713.
60. Lyakhovsky V., Zhu W., Shalev E., Visco- poroelastic damage model for brittle- ductile failure of porous rocks. *J Geophy Res: Solid Earth*. 2015;120:2179-2199.
61. Shalev E., Lyakhovsky V. The role of the intermediate principal stress on the direction of damage zone during hydraulic stimulation. *Int J Rock Mech Min Sci*. 2018;107:86-93.
62. Ben-Zion Y., Lyakhovsky V. Analysis of aftershocks in a lithospheric model with seismogenic zone governed by damage rheology. *Geophys J Int*. 2006;165:197-210.
63. Bauer S.J., Broome S.T., Gardner W. *Release of geogenic gases as a signal of deformation in rock*. in *52nd US Rock Mechanics/Geomechanics Symposium*. 2018. American Rock Mechanics Association.
64. Lei X., Kusunose K., Satoh T., Nishizawa, O. The hierarchical rupture process of a fault: an experimental study. *Phys Earth Planet Interiors*. 2003;137:213-228.

65. Bedford J.D., Faulkner D. R., Leclere H., Wheeler J. High- resolution mapping of yield curve shape and evolution for porous rock: The effect of inelastic compaction on porous bassanite. *J Geophys Res: Solid Earth*. 2018;123:1217-1234.
66. Wong T.-F., Baud P. The brittle-ductile transition in porous rock: A review. *J Structural Geol.* 2012;44:25-53.
67. DiMaggio F.L., Sandler I.S. Material model for granular soils. *J Eng Mech.* 1971.
68. Carroll M. A critical state plasticity theory for porous reservoir rock. *Recent Advances Mech Structured Continua.* 1991;117:1-8.
69. Grueschow E., Rudnicki J.W. Elliptic yield cap constitutive modeling for high porosity sandstone. *Int J Sol Struct*. 2005;42:4574-4587.
70. Stefanov Y.P., Chertov M. A., Aidagulov G. R., Myasnikov A. V. Dynamics of inelastic deformation of porous rocks and formation of localized compaction zones studied by numerical modeling. *J Mech Phys Sol*. 2011;59:2323-2340.
71. Vorobiev O.Y., Liu B. T., Lomov I. N., Antoun T. H. Simulation of penetration into porous geologic media. *Int J Impact Eng*. 2007;34:721-731.
72. Gajst H., Shalev E., Weinberger R., Marco S., Zhu W., Lyakhovsky V. Relating strain localization and Kaiser effect to yield surface evolution in brittle rocks. *Geophys J Int.* 2020;221:2091-2103.

Figure Captions:

Figure 1: Failure regimes for porous rocks.

Figure 2. a) Sample SC-4. Sample is 23.9 mm in diameter and 55.5 mm in height. b) Sample SC-7. Sample is 24.7 mm in diameter and 56.9 mm in height.

Figure 3. Thin section observations of arkosic Zenifim sandstone. Left column is plane light; right column is plane-polarized light. a) Preferential alignment grains. Field of view is 2.04 mm. b) Grains cemented by a fine-grained matrix of hematite, chlorite, and other clays. Field of view 0.8 mm. c) Grains cemented by calcite. Field of view is 0.8 mm.

Figure 4. a) Differential stress versus strain for conventional triaxial experiments. Axial strain is positive, lateral strain is negative. Solid lines are samples cored perpendicular to bedding; dashed lines, parallel to bedding. Experiments conducted at 7 MPa P_C are in red, experiments conducted at 50 MPa P_C are in blue, experiments conducted at 100 MPa P_C are in green, and experiments conducted at 200 MPa P_C are in purple. Only 1 test is shown at 7 MPa and 100 MPa P_C for clarity. b) Differential stress at failure versus mean stress for conventional triaxial experiments, red, and creep tests, green.

Figure 5. Photographs of fractured Zenifim sandstone samples. a) Sample SC-4, deformed at 6.9 MPa P_C. b) Sample SC-7, deformed at 200 MPa P_C.

Figure 6. Differential stress versus strain for a) SC-4 and b) SC-7. Axial components are red, lateral strain is green, and volume strain is blue. LVDT1 values are circles, LVDT2 values are diamonds, SG1 components are dashed lines, and SG2 components are solid lines. Axial stress and cumulative AE hits versus axial strain for c) SC-4 and d) SC-7. Axial stress is in red, AE is in blue. Dashed line marks beginning of creep. Axial strain data for SC-4 is from SG1, and axial strain data for SC-7 is from SG2. Strain is shifted to be 0 at beginning of axial compression.

Figure 7. Axial strain, creep strain rate, lateral strain, volume strain, cumulative AE hits, and AE rate versus time for a) SC-4 and b) SC-7. For SC-4, strain data is from SG1. For SC-7, strain data is from SG2.

Figure 8. High speed axial strain, lateral strain, and volume strain measurements versus time as recorded by the AE system for a) SC-4 and b) SC-7.

Figure 9. Stress – strain curves of the different experiments compared to the calibrated model results. Dotted lines represent the slopes of unloading in experiments and model.

Figure 10. Evolution of strain and yield cap during loading for experiments conducted at a) 50 MPa P_C and b) 100 MPa P_C, and creep experiments conducted at c) 6.9 MPa P_C and 200 MPa P_C.

Figure 11. Evolution during loading with confining pressure of 200 MPa. a) Experimental results of strain and acoustic emission. b) Simulation results of damage and the proximity of the yield cap to the strain state of the rock.

Figure 12. Differential stress versus axial (red), lateral (green), and volume (blue) strain for creep experiments (solid curves) versus conventional triaxial experiments on Zenifim sandstone, (dashed curves). a) Experiments conducted at 6.9 MPa P_C. b) Experiments conducted at 200 MPa P_C.

Table Headings

Table 1. Results for brittle creep experiment on Zenifim sandstone.

Table 2: Calibrated parameters for model.

Figure1

Click here to download Figure fig1.pdf

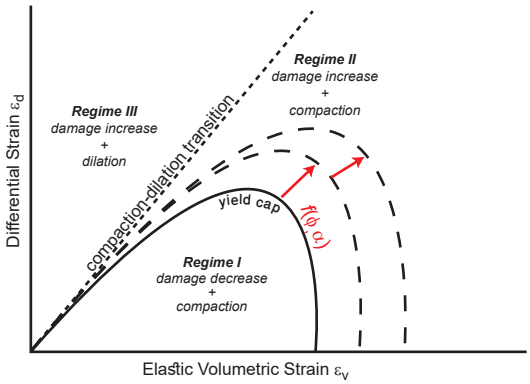

Figure2

Click here to download Figure fig2.pdf

a)

b)

Figure3

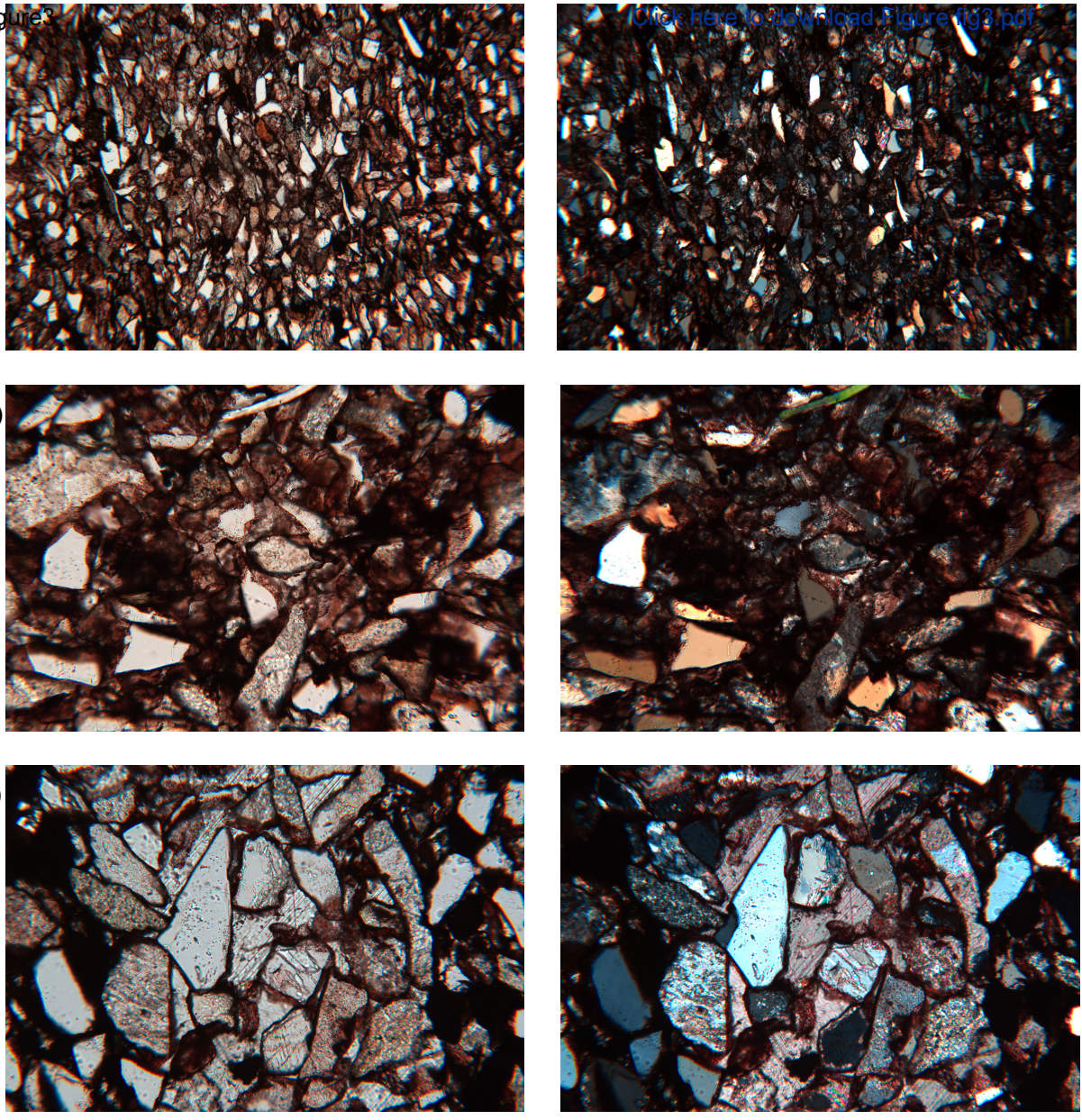

Figure4

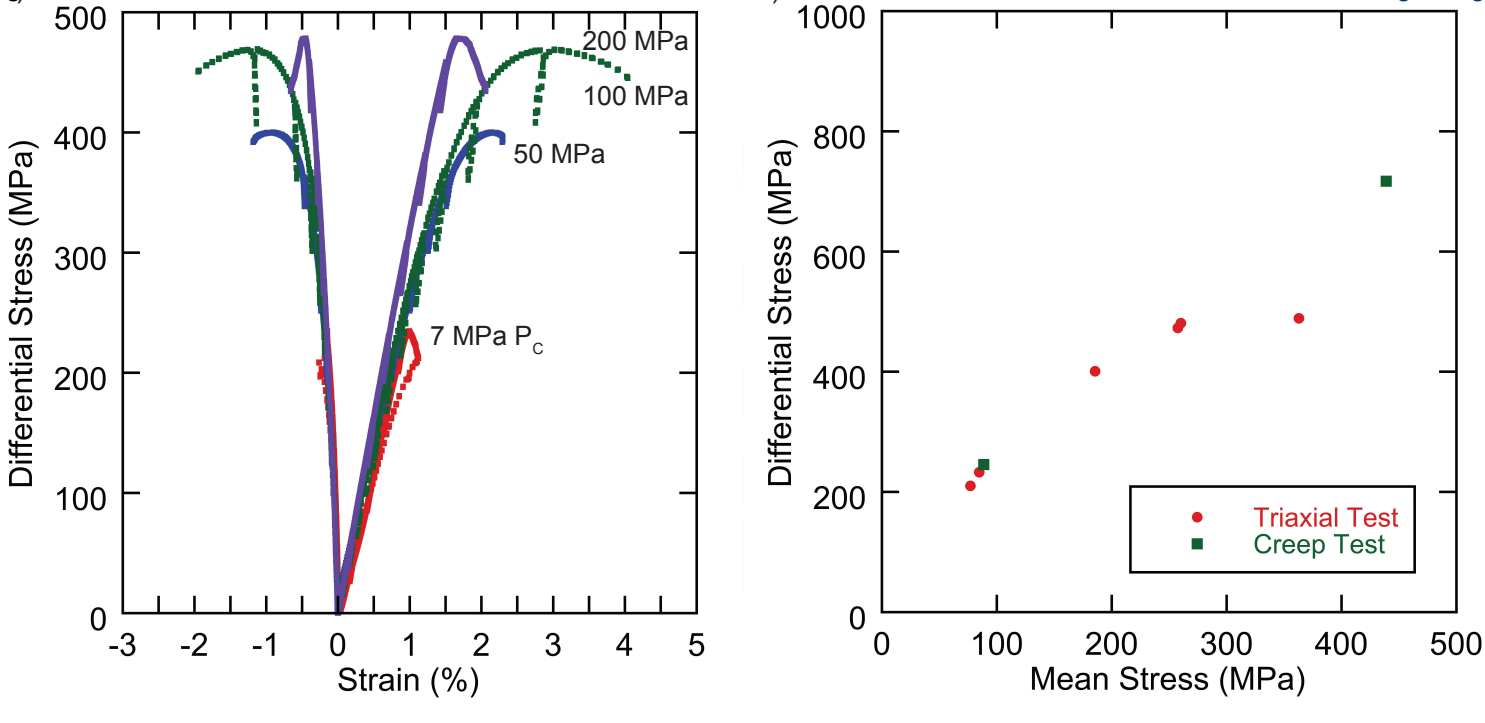

Figure5

Click here to download Figure fig5.pdf

a)

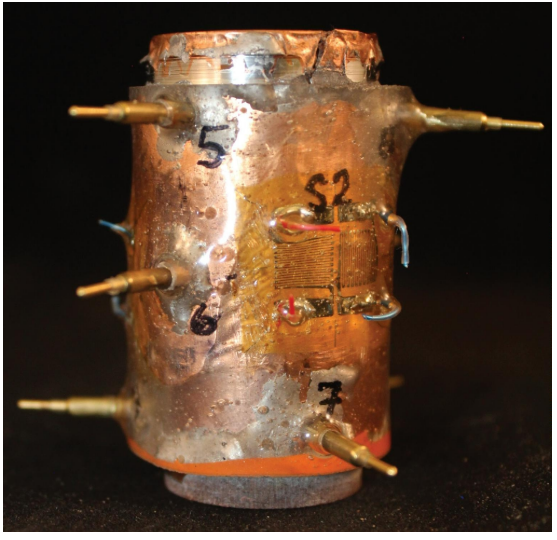

b)

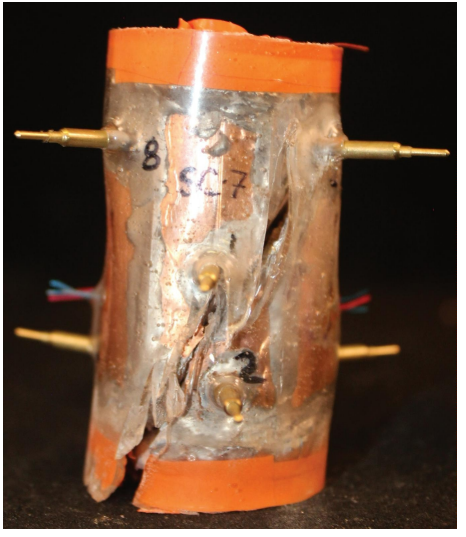

Figure6

Click here to download Figure fig6.pdf

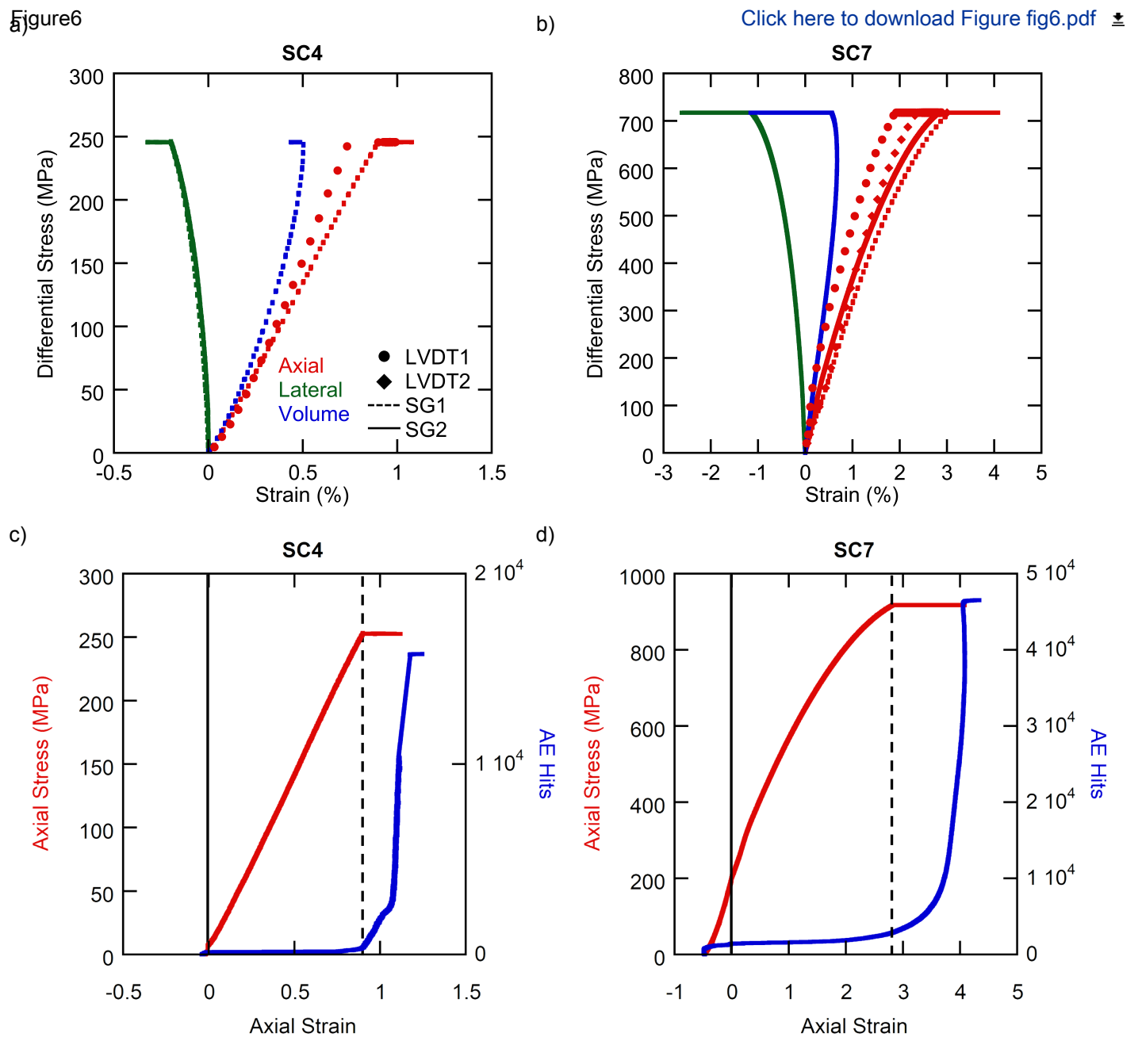

Figure7

Click here to download Figure fig7.pdf

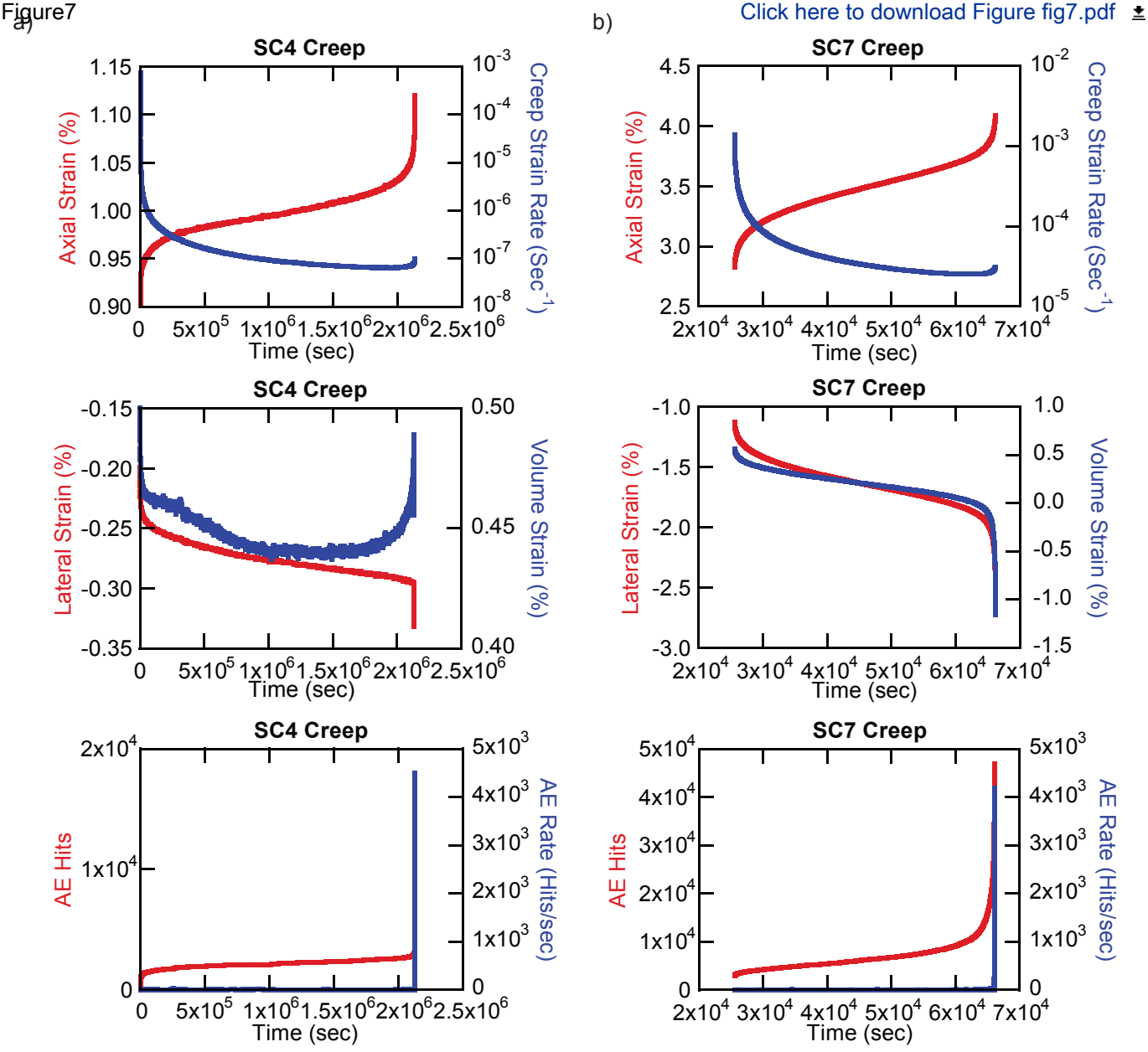

Figure8

Click here to download Figure fig8.pdf

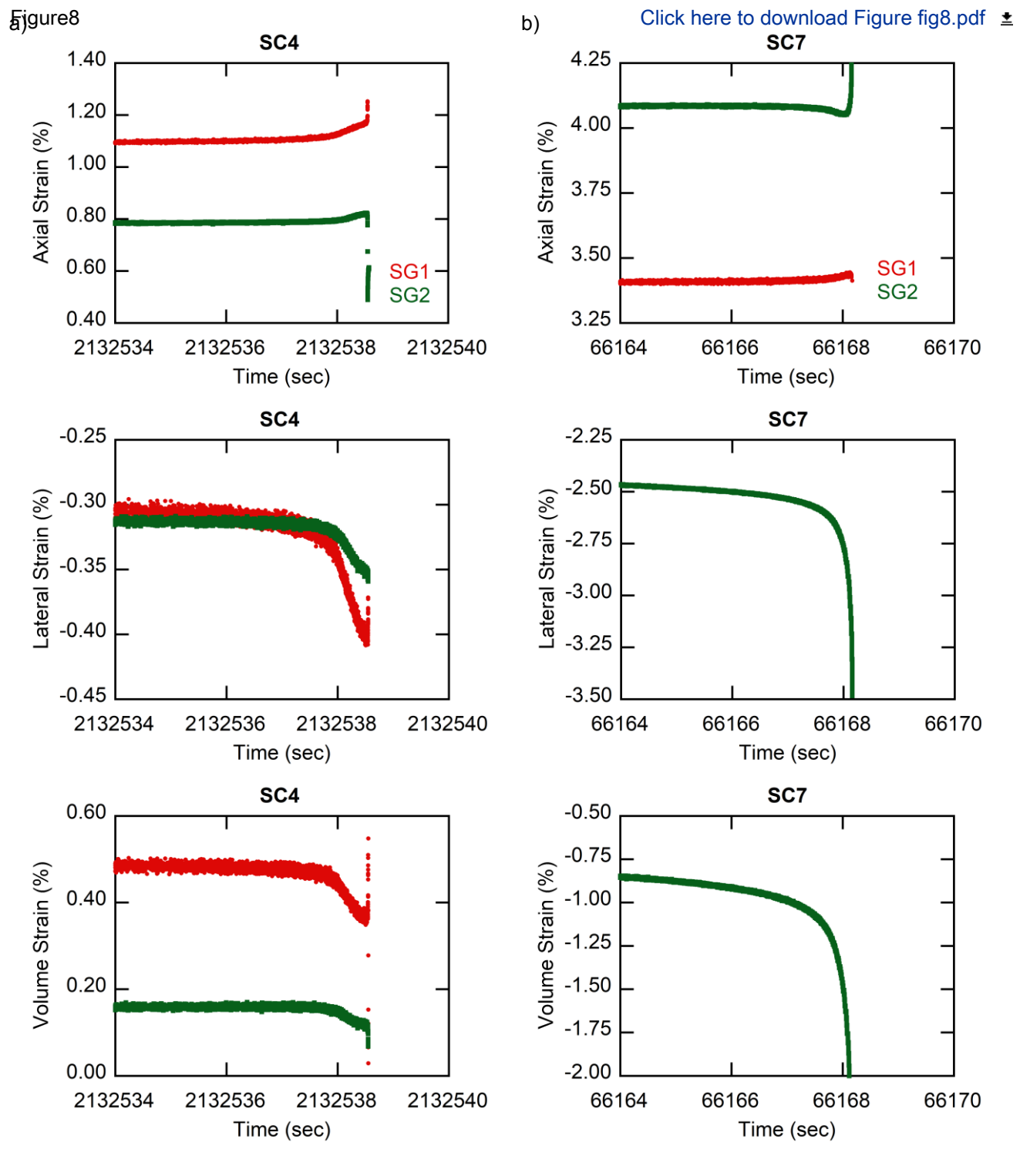

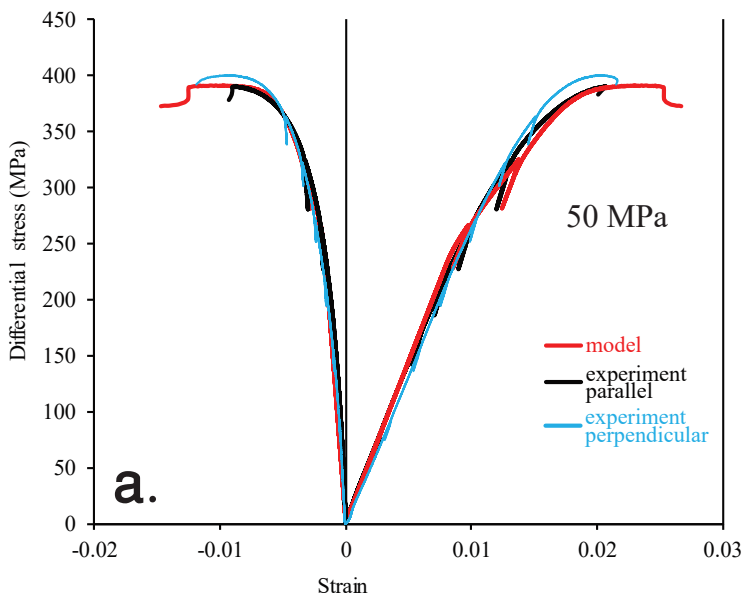

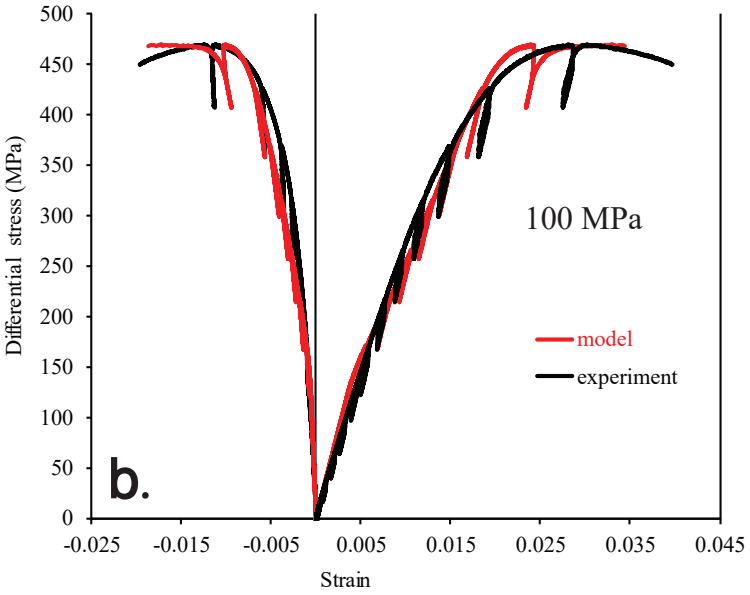

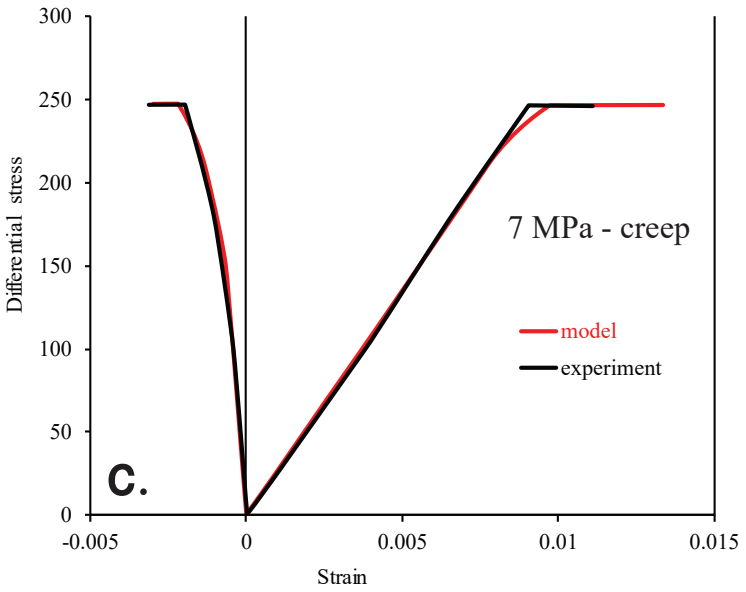

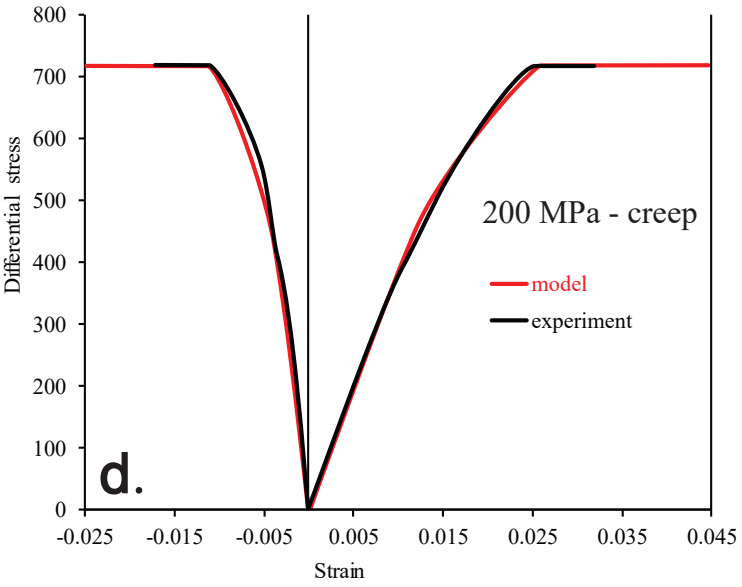

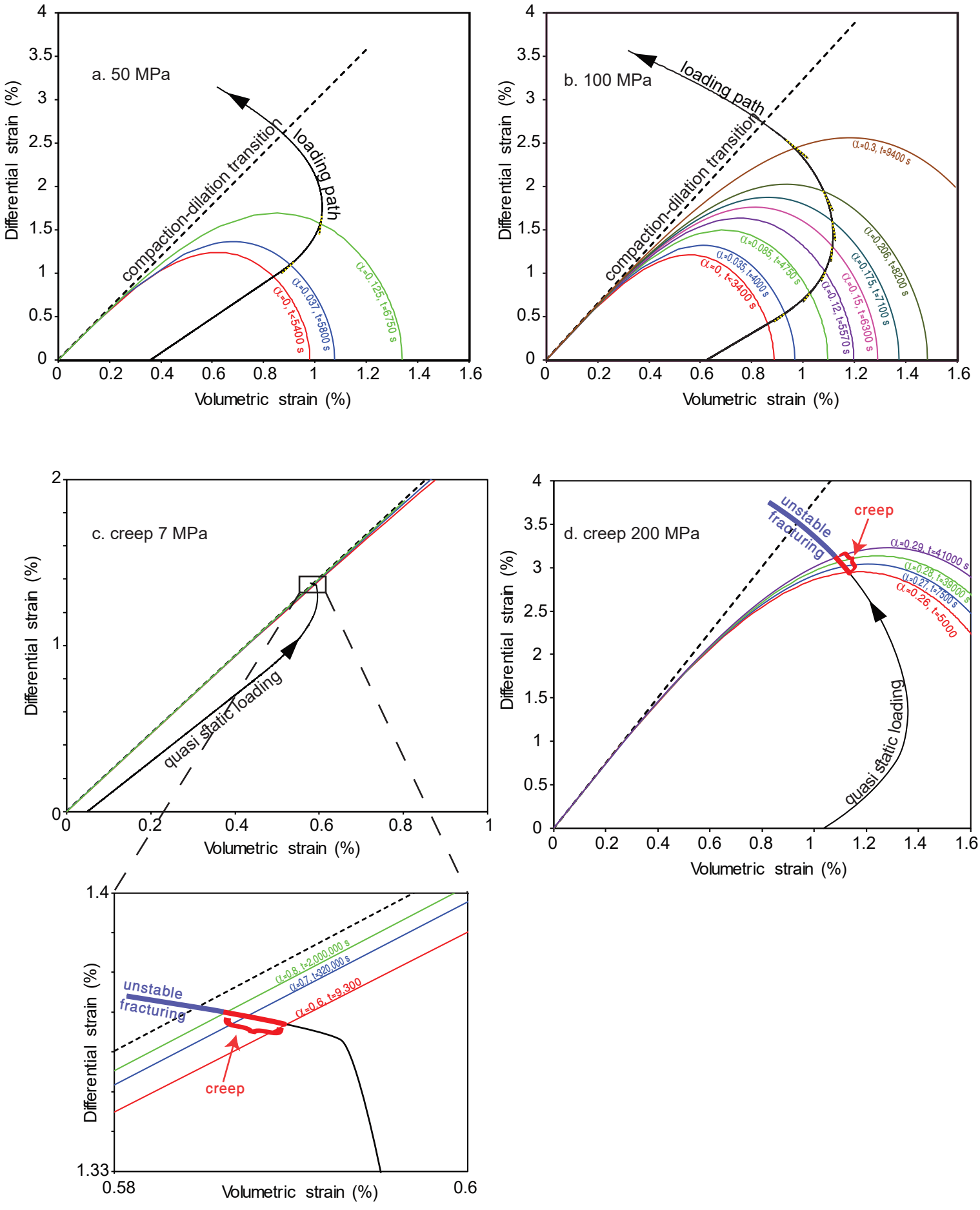

Figure11

Click here to download Figure fig11.pdf

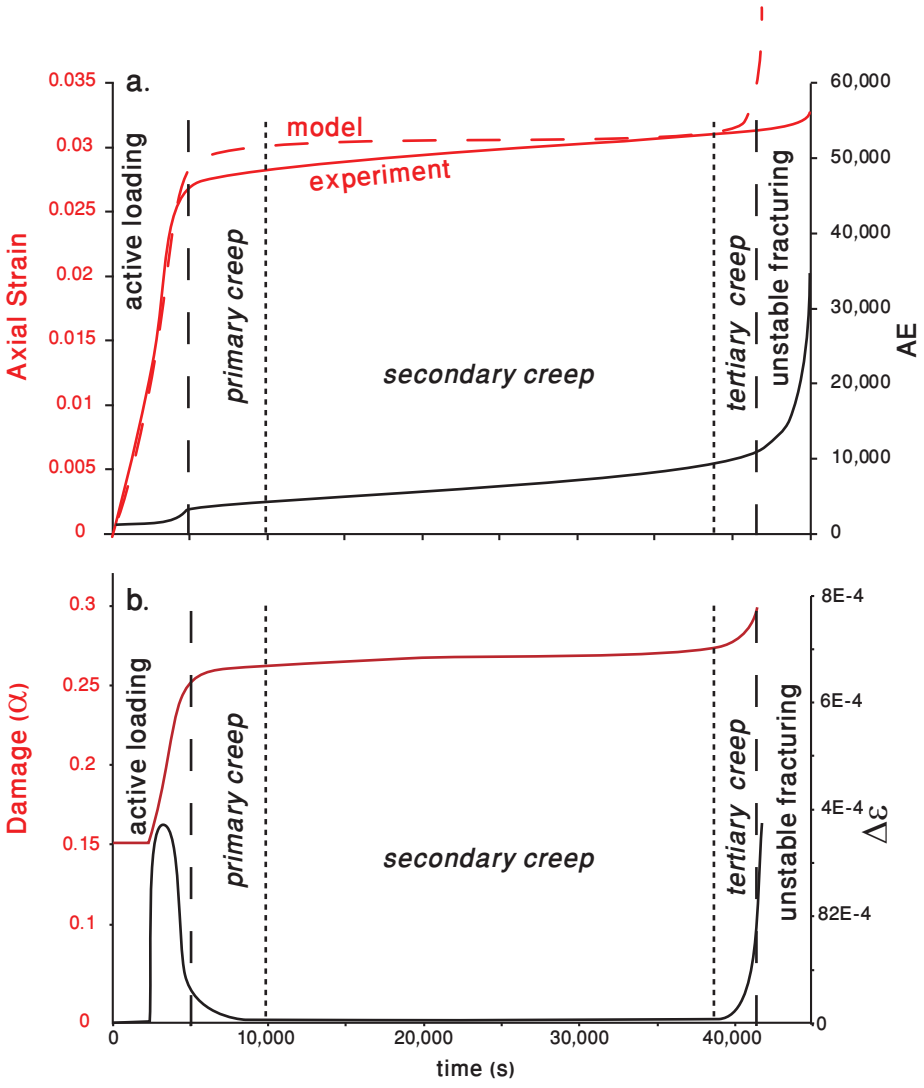

Figure12

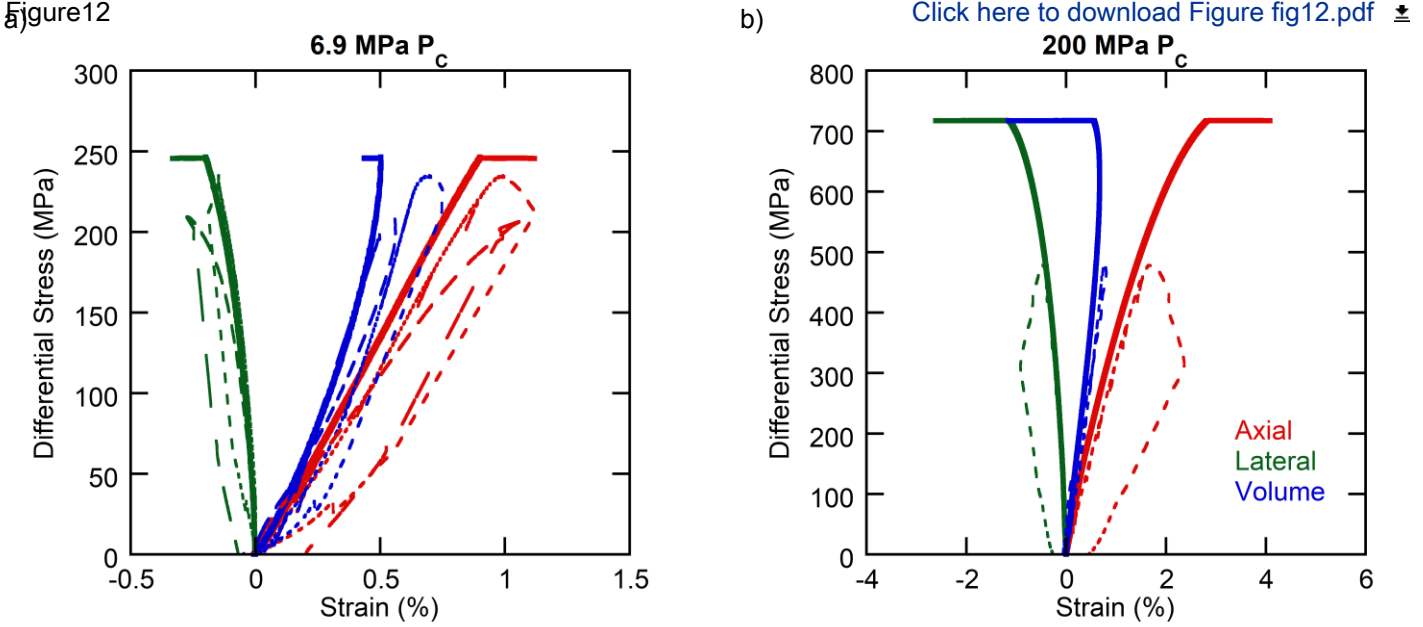

Click here to download Figure fig12.pdf

Table1

Sample	SC-4	SC-7
P_C (MPa)	6.9	200
Creep Stress (MPa)	245.7	717.2
Axial Strain at Failure (%)	1.18	4.34
Lateral Strain at Failure (%)	-0.4	-3.73
Volume Strain at Failure (%)	0.38	-3.11
Time to Failure (sec/hours)	2129659/591.57	40539/11.26
AE Hits at Failure	15762	46498

Table2

Test	Confining pressure	λ MPa	μ MPa	ξ_0	D_1	D_2
2933	100	6000	15000	-0.4	10000	-5
8435 / 8436	50	6000	12000	-0.4	8000	-5
SC-7	200	6000	17000	-0.33	8400	-5
SC-4	6.9	6000	12000	-0.5	8600	-5

Cv 1/MPa	C_d 1/s
2.00E-05	20
2.00E-05	20
2.00E-05	10
2.00E-05	100